

Roughness and near-surface density of Mars from SHARAD radar echoes

Bruce A. Campbell,¹ Nathaniel E. Putzig,² Lynn M. Carter,³ Gareth A. Morgan,¹ Roger. J. Phillips,² and Jeffrey J. Plaut⁴

Received 14 September 2012; revised 12 December 2012; accepted 4 January 2013; published 28 March 2013.

[1] We present a technique for estimating Mars topographic roughness on horizontal scales from about 10 m to 100 m using Shallow Radar (SHARAD) sounding data. Our results offer a view of surface properties complementary to Mars Orbiter Laser Altimeter (MOLA) pulse-width or baseline roughness maps and can be compared to SHARAD peak-echo properties to infer deviations from the average near-surface density. Latitudinal averaging of SHARAD-derived roughness over Arabia and Noachis Terrae shows good agreement with MOLA-derived roughness and provides clear evidence for latitude-dependent mantling deposits previously inferred from image data. In northwestern Gordii Dorsum, we find that bulk density in at least the upper few meters is significantly lower than in other units of the Medusae Fossae Formation. We observe the same behavior indicative of low near-surface density in wind-eroded crater fill in the southern highlands. Combining surface-properties analysis, subsurface sounding, and high-resolution optical images, we show that the Pavonis Mons fan-shaped deposit differs significantly from lobate debris aprons which SHARAD has shown to be ice-cored. There are no internal radar reflections from the smooth-facies portion of the Pavonis Mons fan-shaped deposit, and we suggest that these deposits are either quite thin or have little dielectric (i.e., density) contrast with the underlying terrain. Future application of these techniques can identify other low-density units across Mars, assist in the mapping of regional volatile-rich mantling units, and provide new constraints on the physical properties of the polar layered terrain.

Citation: Campbell, B. A., N. E. Putzig, L. M. Carter, G. A. Morgan, R. J. Phillips, and J. J. Plaut (2013), Roughness and near-surface density of Mars from SHARAD radar echoes, *J. Geophys. Res. Planets*, 118, 436–450, doi:10.1002/jgre.20050.

1. Introduction

[2] The Shallow Radar (SHARAD) sounder on the Mars Reconnaissance Orbiter (MRO) is designed to detect subsurface reflections from dielectric changes associated with geologic interfaces, including the internal layering of the polar deposits. The sounder emits an 85.05 μ s, frequency-modulated (15–25 MHz) chirp to increase the total power in the illuminating signal and recovers a fine resolution in time delay by correlating the received echoes with a model for the transmitted waveform. The SHARAD signal spans a free-space wavelength range of 20 m (at 15 MHz) to 12 m (at 25 MHz). The 10 MHz bandwidth yields a one-way range resolution in vacuum of 15 m, corresponding to a vertical resolution

of 5–8 m in typical Martian materials. Focused synthetic-aperture processing is used to increase the coherent gain of the returned signals and narrow their along-track resolution to 300–500 m [Seu *et al.*, 2007]. SHARAD echoes also contain information on the roughness and dielectric properties of Mars, the range between the spacecraft and surface, and the total electron content of the intervening ionosphere [Campbell *et al.*, 2011; Safaeinili *et al.*, 2007]. Here we focus on the recovery of surface physical properties from the peak power and delay width of the SHARAD echoes.

[3] The term “roughness” is used here to describe the statistical variation of surface elevation, or the distribution of slopes between adjacent discrete samples of the topography, over a specified horizontal length scale. Both parameters often change in a power-law fashion with horizontal scale; the root mean square value of elevation samples typically rises as the length scale increases, while the rms value of facet slope declines [e.g., Shepard *et al.*, 2001]. Some techniques, such as laser altimetry or stereo photogrammetry, directly sample the surface elevation at some horizontal posting and vertical resolution. Other methods, such as laser pulse-width estimation or radar remote sensing, can characterize the slope distribution and reflectivity of a surface but only through model-dependent interpretations [e.g., Hagfors, 1964; Barrick

¹Center for Earth and Planetary Studies, Smithsonian Institution, Washington, D.C., USA.

²Southwest Research Institute, Boulder, Colorado, USA.

³NASA Goddard Space Flight Center, Greenbelt, Maryland, USA.

⁴Jet Propulsion Laboratory, Pasadena, California, USA.

Corresponding author: Bruce A. Campbell, Center for Earth and Planetary Studies, Smithsonian Institution, MRC 315, PO Box 37012, Washington, D.C. 20013-7012, USA. (campbellb@si.edu)

©2013. American Geophysical Union. All Rights Reserved.
2169-9097/13/10.1002/jgre.20050

and Peake, 1967; Simpson and Tyler, 1982; Ford and Pettengill, 1992; Simpson et al., 1992; Shepard et al., 1995; Neumann et al., 2003; Mouginot et al., 2009; Grima et al., 2012]. We derive here a parameter from the SHARAD echoes related to the rms slope of the surface on horizontal scales between about 10 m and 100 m, based on earlier work related to radar scattering in the near-nadir regime. These roughness values are then used to make qualitative observations regarding the role of Fresnel reflectivity changes in modulating the surface radar echo.

[4] There are two prior sources of information on the global-scale roughness properties of Mars, both based on measurements from the Mars Orbiter Laser Altimeter (MOLA). The altimeter observations include an estimate of the reflected-signal pulse width, which is related to the roughness of the surface over laser footprints of about 75 m diameter. The horizontal and vertical scales of the sensed roughness are not well constrained but are likely of order 1 m [Neumann et al., 2003]. Very smooth surfaces (rms vertical deviations of <1 m over the footprint) cannot be further differentiated, and gaps in valid data coverage limit the spatial resolution of the global dataset to $\frac{1}{4}$ degree (~ 15 km). The MOLA radius measurements for Mars were also used to generate estimates of topographic roughness over baseline lengths from 600 m to about 20 km [Kreslavsky and Head, 2000]. The finest scale is defined by the typical 300 m along-track spacing of the MOLA laser footprints, and the spatial sampling of the output maps is set to about 15 km in order to adequately sample statistical fluctuations in surface height. Both products show the rugged structure of dune fields surrounding the polar layered deposits, the textures of lava flows from major volcanoes, and patterns of latitude-dependent roughness linked with potentially volatile-rich mantling deposits [Kreslavsky and Head, 2002].

[5] Local measurements of surface roughness can be derived from the behavior of the SHARAD echo as a function of time following the initial strong surface peak [e.g., Hagfors, 1964], with averaging over about 3 km in the along-track direction to reduce speckle and clutter uncertainties. The overall density of spatial sampling within a region is set by the degree of SHARAD track coverage, which is not uniform across the planet. SHARAD roughness measurements are sensitive to topographic statistical behavior on horizontal scales (10–100 m) about an order of magnitude below that of the finest MOLA point-to-point analyses and 1–2 orders of magnitude above those related to the MOLA pulse-width variations. The SHARAD echoes are also sensitive to slight changes in surface roughness at the relevant spatial scales and thus provide greater discrimination than the pulse-width measurements among plains units and other relatively smooth regions.

[6] We first describe the SHARAD dataset and the steps involved in our synthetic-aperture processing (section 2). In section 3, we review radar scattering models applicable to observing geometries within a few degrees of normal incidence, providing the rationale for our roughness estimation technique. We also point out that the roughness parameter is affected by subsurface reflections and scattering, and that this might enable the detection of shallow (<30 m) interfaces or physical properties. In section 4, we present maps of roughness and peak SHARAD echo strength for a variety of settings on Mars and discuss their importance

for understanding geologic processes. In section 5, we summarize these results and discuss further applications of our technique.

2. SHARAD Data

2.1. Sampling Format

[7] Each SHARAD measurement, or echo record, comprises 3600 real-valued samples of received voltage, and these data are transmitted to Earth after analog-to-digital (A/D) conversion. The range of the A/D conversion is adjusted, by reference to the signal-level distribution, to properly sample the system noise and the received echoes from Mars with minimal clipping. The received voltages are sampled at $0.0375 \mu\text{s}$ intervals, forming a “delay window” 135 μs in duration. This corresponds to only 20.25 km in one-way path length through free space, and since topographic variations on Mars approach 30 km, the beginning of the delay window must be shifted to capture the echo from the surface and reflections from several kilometers below the surface (Figure 1). The delay-window start time, with respect to

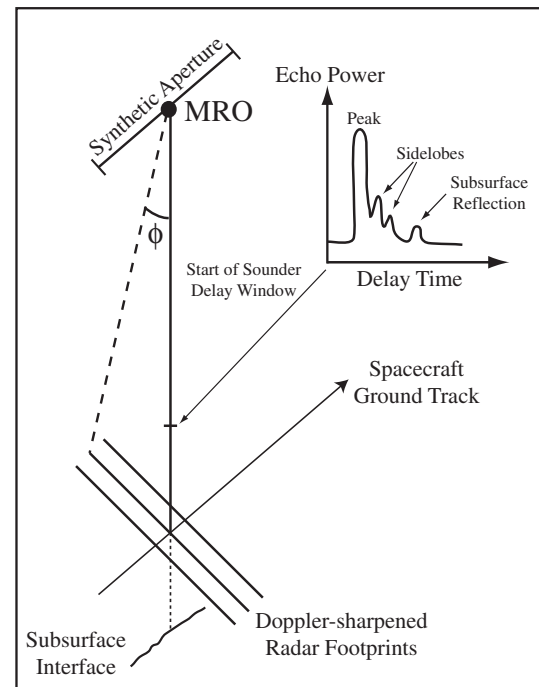


Figure 1. Cartoon of SHARAD sounding operation and a typical pulse record. Each radar pulse initiates a recording cycle whose start time is set to allow a small delay window before the surface return. Processing numerous such pulse records over a period of time defined by the synthetic aperture allows for a much narrower footprint in the along-track dimension. Echoes from the surface come from a region perpendicular to the center of each posted radargram record. The incidence angle ϕ between the transmitted signal and a plane reference surface increases with distance from the ground track. The peak echo comes from mirror-like scattering close to the sub-spacecraft point, with sidelobes due to Fourier-transform processing that is required to yield a narrow pulse from the original chirp.

the initiation of each transmit cycle, is adjusted every 64 echo records by reference to a stored model of Martian topography [Seu *et al.*, 2007; Croci *et al.*, 2011].

[8] Pulses are transmitted and received with a repetition frequency of 700.28 Hz. Because allowed data volume for transmission to Earth is limited, SHARAD performs onboard coherent presumming of echo records, typically by a factor of 4 or 8. While presumming narrows the Doppler bandwidth of the received-signal spectrum, the orbital geometry and range of SHARAD operating frequency make it unlikely that even the eightfold compression will create aliasing in the echo spectrum. Data delivered to investigators has been converted to an 8 bit format, with the effects of the automated A/D range operation compensated to provide a nominally uniform power reference.

2.2. Range Compression

[9] To achieve the desired signal-to-noise performance for radar sounding, SHARAD employs a linear frequency-modulated chirp signal. The digital electronics deliver a uniform excitation to the power amplifier, but the actual transmitted signal differs substantially from a flat amplitude behavior with frequency. The SHARAD antenna is a 10 m dipole, and even with a matching network its effective gain shifts by up to 50% over the 10 MHz chirp. This amplitude ripple is modestly affected by instrument temperature. A narrow pulse in delay time is recovered by correlating the received signal for each echo record with a model for the transmitted chirp in a process termed “range compression.” In detail, we take the Fourier transform of the 3600 voltage samples, multiply by the complex conjugate of the Fourier transform of the chirp model, multiply one half of the spectrum by zero, and inverse Fourier transform to create a complex-valued output array. A windowing filter, such as a Hann function, is applied in the frequency domain prior to the inverse transform to reduce the sidelobe level in the compressed echo. The resulting 3600 samples represent a twofold over-sampling of the complex echo values, but we retain the larger array size to minimize later issues with interpolation along an echo record. The band-limited sampling arrangement used in the SHARAD data acquisition fully aliases the spectrum, so the frequency indexing of the transformed echoes is reversed from the typical Fourier-transform format [Croci *et al.*, 2011]. Due to the amplitude changes with frequency induced by the antenna and matching network, using a linear chirp model as we do in our range compression can yield results that are sub-optimal for some applications. Use of the linear chirp leads to an asymmetric offset of the characteristic transform sidelobes, with greater sidelobe power on the down-range (greater delay) side of any echo. While this effect can nominally be compensated by prelaunch measurements of the system behavior, our analysis method for the near-nadir scattering behavior (section 3) relies on a consistent sidelobe behavior rather than symmetry, so we have not pursued additional corrections.

2.3. Rolled Observations

[10] The dipole antenna is mounted parallel to the flight direction of MRO and high along one side of the spacecraft bus. The presence of the bus and solar panels in the near field significantly distorts the beam pattern, and roll maneuvers up to about a 25° angle can be performed to bring the peak of

the beam pattern closer to nadir. In these “rolled” observations and with the solar panels placed in an empirically derived configuration to minimize their impact, the signal-to-noise ratio (SNR) of any given reflector may increase by up to 6 dB over the nominal, nadir-pointed spacecraft geometry.

2.4. Synthetic Aperture Processing

[11] A single SHARAD echo record may contain reflections from the surface and subsurface, but the broad antenna pattern combines returns from a large cross-track and along-track footprint and yields only a modest SNR for typical reflectors. Both resolution and SNR are improved by synthetic-aperture processing. There are a variety of methods to implement the required resampling of the echoes in delay (range migration) and the compensation of phase (range-rate) variations over a coherent integration period or synthetic aperture. We describe below the specific steps used in our processing.

[12] The synthetic aperture is composed of individual echo records for some number of sequential observations, typically 10 s to 40 s in total duration. For MRO tangential velocities, the corresponding apertures span a distance of about 30 km to 130 km in the along-track direction. To begin processing, the range-compressed data are assembled into a two-dimensional, complex-valued array, with round-trip delay along the vertical axis and along-track time on the horizontal axis. The first step in our processing is range migration, which aligns the delay locations in every echo record corresponding to a point on the surface at the center of the physical aperture. For the center record, there is thus no migration, and other echo records are shifted progressively uprange (since the center point appears at greater distance from the sensor) with increasing separation. Along any cut through the along-track time axis, the samples will now correspond to reflections from a point target or a planar feature with no tilt in the along-track dimension. To the extent the surface or subsurface reflectors have a slope in the along-track axis, this step will misalign those signals and lead to blurring or artifacts in the final *radargram* (image-format displays of signal power with round-trip delay time on the vertical axis and along-track distance on the horizontal axis). There is a potentially important variation in the required delay shift with separation from the aperture center as the depth to a reflector increases. In “omega-k” (frequency-wave number) processing [Cumming and Wong, 2005], the range samples are interpolated to compensate for variation with distance, but our processing employs only a surface point-target model. Use of this simplification is based on our experience that the focusing is not significantly depth dependent, and it avoids two-dimensional interpolation that may create undesired artifacts.

[13] The second processing step exploits Doppler-shift information contained in the phase of signals, relative to the point-target location, as the spacecraft moves through the physical aperture. Our processor uses the altitude, radial velocity, and tangential velocity information provided by the MRO SPICE (Spacecraft Planet Instrument Camera-matrix Events) kernels to determine a differential phase (with respect to the aperture center) for each echo record. No significant variation is assumed to occur within any single record, and the phase function is based on the behavior of a point target at the MOLA-specified elevation of the surface. In principle, the phase correction can be applied as a function of frequency across the chirp bandwidth, but we find that good focusing

performance is achieved by a single-valued phase correction scaled to the highest frequency component (25 MHz). After the phase correction is applied, one vertical column of the radargram is produced by Fourier-transforming range-migrated “lines of equal delay” and taking the magnitude (or power) of the resulting frequency spectrum. Properly range-migrated and phase-compensated reflections from various targets are thereby summed coherently to achieve substantial improvement in SNR. The isolation of the frequency components also serves to narrow the along-track resolution of the sensor by excluding echoes from targets beyond some limiting Doppler shift. We post radargram columns at 128 points per degree spacing (about 460 m along track).

[14] The output power value in each range cell of this radargram column is a summation over a chosen Doppler-frequency range about the zero-Doppler center of the spectrum. If the Doppler bin is wide enough to include more than one frequency resolution cell (whose width is determined by the inverse of the total duration of the synthetic aperture), then a multi-look product is created with reduced speckle uncertainties. After multi-look processing, there is no frequency or phase information; the radargram is purely a measure of echo power. Ionospheric compensation for observations at solar zenith angles $<100^\circ$ is implemented per *Campbell et al.* [2011]. For consistency, we use a fixed synthetic-aperture length of 11 s, a multi-look frequency window of 0.2 Hz, and Hann windowing for sidelobe reduction in the range-Doppler processing of all sounder tracks.

2.5. Clutter

[15] Within a single radargram, echoes from parts of the surface (or subsurface) that lie away from the nadir track but are perpendicular to the Doppler-sharpened frequency resolution cell cannot be readily discriminated from nadir subsurface reflections. These interfering echoes are termed clutter and may be attributed to two mechanisms. The first source of echoes is “deterministic” features, such as hill-sides, crater walls, and other large topographic features with local orientation perpendicular to the incident radar signal. These features can often be identified by comparison with simulated radargrams produced by ray tracing of a digital terrain model. The second source of clutter is random roughness on the topographic scales that affect scattering at SHARAD frequencies. This style of roughness leads to diffuse reflected power that decreases with time after the surface return, and the behavior of the decay is used in section 3 to infer surface roughness.

3. Characterizing Surface Roughness from SHARAD Echoes

[16] SHARAD measures radar echoes from the surface of Mars between nadir (normal incidence) and a maximum incidence angle, ϕ , of about 20° (Figure 1). In this regime, radar backscatter may arise from coherent scattering where the surface is smooth to a fraction of the incident wavelength over much of the illuminated footprint or by incoherent scattering from smaller, mirror-like facets with a distribution of tilts [e.g., *Barrick and Peake*, 1967]. The mirror-like or quasi-specular facets must be smooth on horizontal scales of about 1/10 the illuminating wavelength. At the center

wavelengths used by the MARSIS subsurface probing bands (60 m to 166 m), the assumption of a horizontal, planar reflecting interface is reasonable for many regions, and coherent scattering is expected. At SHARAD wavelengths (12 m to 20 m), surface roughness likely disrupts coherent behavior, so this mechanism only occasionally generates brighter returns from smooth patches [*Campbell and Shepard*, 2003]. Our model for estimating surface roughness therefore assumes only scattering by facet-like patches that sum incoherently.

[17] Echoes from quasi-specular facets over the illuminated area exhibit an angular scattering behavior that depends only on the Fresnel normal reflectivity ρ and a “roughness” term, the rms slope s that captures the angular width of the tilt distribution [*Hagfors*, 1964] (Figure 2). Roughness on geologic surfaces often will not have a dominant spatial wavelength, so the horizontal scale to which s applies can only be inferred as being within the range from about the radar wavelength to some significant fraction of the illuminated footprint. For SHARAD, this corresponds to length scales on the order 10 m to 100 m. As found from radar and photogrammetric studies of the Moon, the horizontal scale at which a radar-derived s value and the actual topographic rms slope coincide can vary with landform structure [*Tyler*, 1979]. This suggests that a roughness parameter derived from near-nadir scattering behavior represents the aggregate response of the surface over the relevant range of horizontal scale.

[18] There are numerous models for incoherent scattering based on the statistical distribution of mirror-like surface facets. The shape of that tilt distribution may be Gaussian, exponential [*Simpson and Tyler*, 1982], or a hybrid form [*Hagfors*, 1964]. All of these forms may be special cases within a framework provided by self-affine surface statistics [*Shepard et al.*, 1995]. Incoherent scattering models share two attributes that are useful in extracting surface properties. First, the ratio of the integrated power, P_i , over some chosen

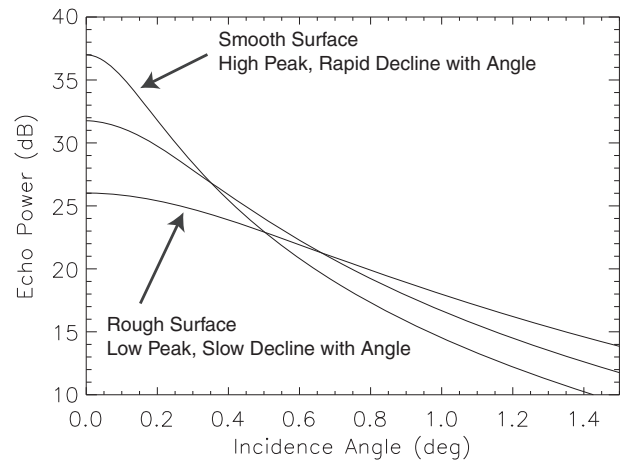


Figure 2. Plot of backscatter coefficient versus radar incidence angle for three values of the surface rms slope, using the model of *Hagfors* [1964]. Our roughness technique exploits the fact that rougher surfaces have greater integrated backscattered power, relative to their peak echo, than smooth surfaces.

range of radar incidence angle ϕ , to the peak power is independent of ρ

$$\frac{P_i}{P_o} = \frac{\int_0^\Phi \sigma^o(\phi) d\phi}{\sigma^o(0)} \quad (1)$$

and thus modulated only by s . The parameter σ^o is the dimensionless backscatter coefficient. This ratio is also insensitive to changes in the echo power due to changes in the system gain with antenna orientation, MRO solar panel position, or ionospheric attenuation.

[19] Taking the functions of *Simpson and Tyler* [1982] and dividing each by a $\cos(\phi)$ term to correct for effective scattering area yields the relationship between “integrated” and “peak” backscattered power for various slope distributions:

$$\left(\frac{P_i}{P_o}\right)_{\text{Gaussian}} = \int_0^\Phi \sec^4 \phi \exp\left[\frac{-\tan^2 \phi}{s^2}\right] d\phi \quad (2)$$

$$\left(\frac{P_i}{P_o}\right)_{\text{Exponential}} = \int_0^\Phi \sec \phi \exp\left[\frac{-\tan \phi}{s}\right] d\phi \quad (3)$$

$$\left(\frac{P_i}{P_o}\right)_{\text{Hagfors}} = \int_0^\Phi \left[\cos^4 \phi + \frac{\sin^2 \phi}{s^2}\right]^{-1.5} d\phi \quad (4)$$

[20] The relationship between the ratio in equation (1) and s depends only modestly upon the statistical form of the quasi-specular facet distribution. Figure 3 shows calculated values for the three distributions for an ideal case without echo sidelobes but with the appropriate spacing of incidence-angle bins to match SHARAD sampling. The maximum rms slope is taken to be 10° , based on studies of natural surfaces at the 10 m horizontal scale [*Shepard et al.*, 2001]. At very low roughness, the ratio remains near unity until the angular width of the surface echo exceeds the incidence-angle width of the first delay bin. The three models yield similar

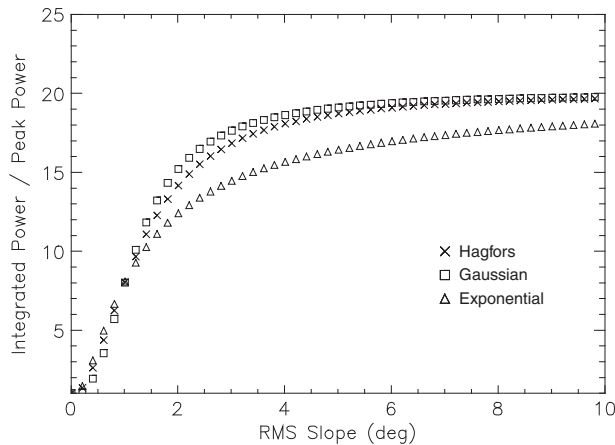


Figure 3. Ratio between integrated radar echo, from 0° to 1.5° incidence angle, and peak nadir reflection as a function of rms slope for three surface-facet statistical distributions (Hagfors = crosses, Gaussian = squares, Exponential = triangles). The roughness parameter inferred from SHARAD echoes is relatively insensitive to the form of the slope distribution, and so is a reasonable proxy for surface rms slope at horizontal scales between about 10 m and 100 m.

results to about 1° rms slope and diverge by about 15% from an average value when the rms slope is $>2^\circ$. We thus present the ratio value in equation (1) as a *roughness parameter* ζ that serves as a proxy for rms slope at horizontal scales between about 10 m and 100 m, with the caveat that minor differences between geologic units may reflect variations in either rms slope or facet distribution.

[21] A second attribute of incoherent scattering models is that the peak response depends linearly on the Fresnel normal reflectivity and the inverse square of the rms slope:

$$P_o \propto \left(\frac{\rho}{s^2}\right) \quad (5)$$

[22] In principle, we could use the roughness term estimated from the ratio of integrated to peak power (equation (1)) to normalize the peak echo and examine residual variations associated with surface reflectivity (i.e., dielectric constant) changes. This analysis, however, depends to a much larger degree than the roughness estimate upon accurate calibration of the SHARAD echoes. The effective gain of the sounder varies with the pointing angle of the antenna with respect to nadir, the positions of the spacecraft solar panels and high-gain antenna, the altitude of the observation, and the degree of attenuation induced by the ionosphere [e.g., *Grima et al.*, 2012]. Even after these variations are corrected, there may be surges in echo strength from very smooth terrain due to coherent scattering [*Campbell and Shepard*, 2003]. The uncertainties introduced by calibration, the specific form of the near-nadir scattering mechanism (Figure 3), and regional slopes may overwhelm the relatively small variation in Fresnel reflectivity (from perhaps $\rho = 0.05$ to $\rho = 0.25$) due to surface density or composition. Thus, we only present maps of relative deviations in peak-echo power and comment on correlations between reflectivity and geologic units.

[23] For each focused echo record in a radargram (Figure 4, top panel), we determine the peak-echo (greatest power) location in delay and shift the data to place this peak at the center of the range window (Figure 4, center panel). We average the resulting dataset using a seven-sample (3.22 km along track) boxcar filter to mitigate the impact of isolated clutter features. To calculate the roughness parameter ζ , we take the ratio of total power in the first 20 delay bins (0.713 μ s in round-trip delay) to the peak-echo power (Figure 4, bottom panel). This corresponds to radar echoes from the surface between nadir and 1.5° incidence angle, identical to the range used for the examples in Figure 3. This range was chosen partly due to the rapid decline in quasi-specular power with angle for most surfaces, and partly to avoid many of the subsurface reflecting horizons noted in volcanic and sedimentary deposits across the equatorial region of Mars [e.g., *Campbell et al.*, 2008].

[24] In our derivation of the roughness parameter, we assume that all of the radar returns arise from topographic variations in a strip of terrain perpendicular to the spacecraft ground track and extending about 8 km (for a 0.713 μ s delay at 300 km spacecraft altitude) to either side of the nadir point (Figure 1). The observed power can also include echoes from dielectric interfaces or objects beneath the surface. For materials with a dielectric constant of 3 to 9, the integrated power will include returns due to layering or volume scattering from depths of 60 m to 35 m, respectively. Whatever their source, subsurface echoes will increase the apparent

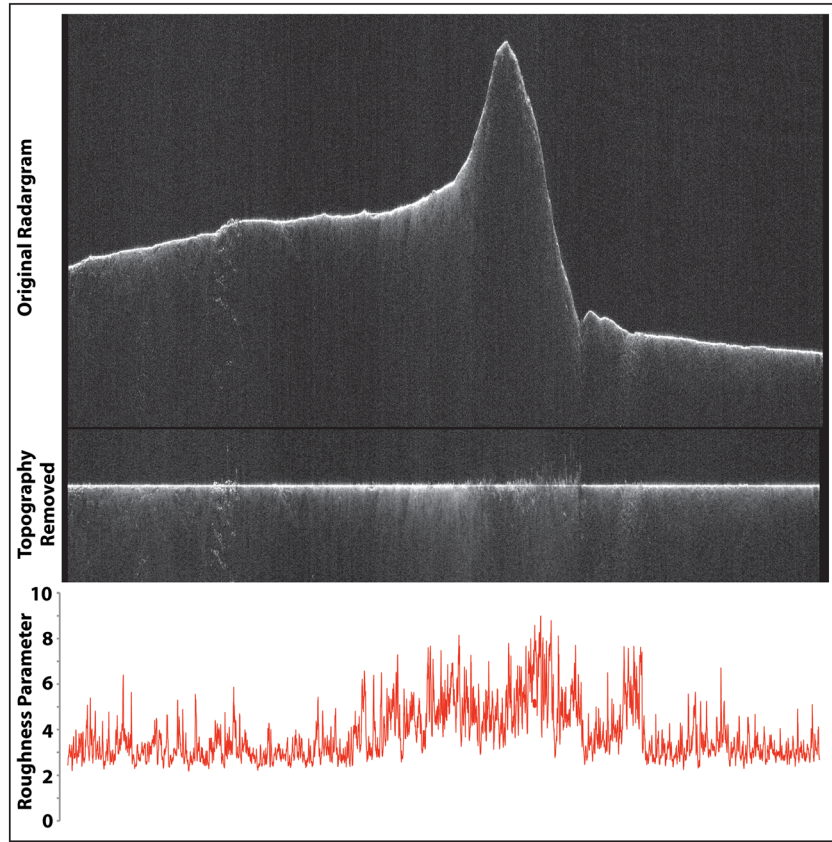


Figure 4. Illustration of roughness derivation from a SHARAD radargram. Original radargram (top panel), in this case for track 1962801 over Pavonis Mons, is adjusted to bring each echo peak to the same range cell (center panel). The roughness parameter (lower panel) is calculated from the ratio of the integrated power in the first 20 range cells to the peak power. Note the correlation between higher roughness values and brighter “waterfall” patterns of scattered power in the radargrams.

surface roughness derived using equation (1). There could also be an impact on radar scattering properties if the near-surface geologic setting includes planar layering of closely spaced dielectric interfaces. In this scenario, interference effects can play a major role in the radar echo, as suggested for MARSIS observations of the south polar deposits by *Mouginot et al.* [2009]. It seems unlikely that such extensive smooth interfaces and narrow range of layer thicknesses occur on the spatial scales relevant to SHARAD probing of the Martian equatorial region.

4. Roughness and Reflectivity Variations among Geologic Units

[25] Here, we restrict our analysis to geologic features between 70°S and 70°N latitude. We also omit the approximately 500 tracks collected in the rolled configuration to avoid confusion in studies of relative surface reflectivity changes. Within this region, we obtain about 13 million roughness footprints from the nadir-oriented sounding tracks. Areas at higher latitudes have interesting variations in surface roughness, as is clear from MOLA results [*Kreslavsky and Head*, 2000, 2002] and preliminary SHARAD mapping [*Campbell and Putzig*, 2011]. However, interpretation of results from the technique described in section 3 is complicated for the polar layered deposits by the occasional occurrence of

subsurface reflectors that are brighter than the initial surface echo and by the potential interference effects noted by *Mouginot et al.* [2009]. For these areas, topographic data must be used to avoid misidentification of the nadir return.

4.1. Global and Regional Properties

[26] SHARAD spatial coverage through MRO orbit 25999 is relatively dense for the Amazonis and Elysium Planitiae regions, the Tharsis Montes, and targeted areas around past (e.g., Meridiani Planum) or candidate landing sites (Figure 5). The roughness parameter ζ has a distribution from about 2 to 8, with a mean value over the study region of about 3 (Figure 6). For each footprint of this map, we also determine an average peak backscatter in decibels, relative to an arbitrary reference. The noise floor of the instrument is about -55 dB for the processing parameters discussed in section 2. Figure 7 shows the distribution of peak values (dashed curve) for the entire study region, which has a standard deviation of about 5.3 dB. We examined the behavior of the peak-echo strength as a function of roughness and found that over the range of $\zeta = 2$ –10, a good fit is obtained with the following :

$$P_0(\text{dB}) = -15.64 - 2.85\zeta(\text{dB}) \quad (6)$$

[27] The solid curve in Figure 7 shows the distribution after compensating each peak echo by the slope term in this expression.

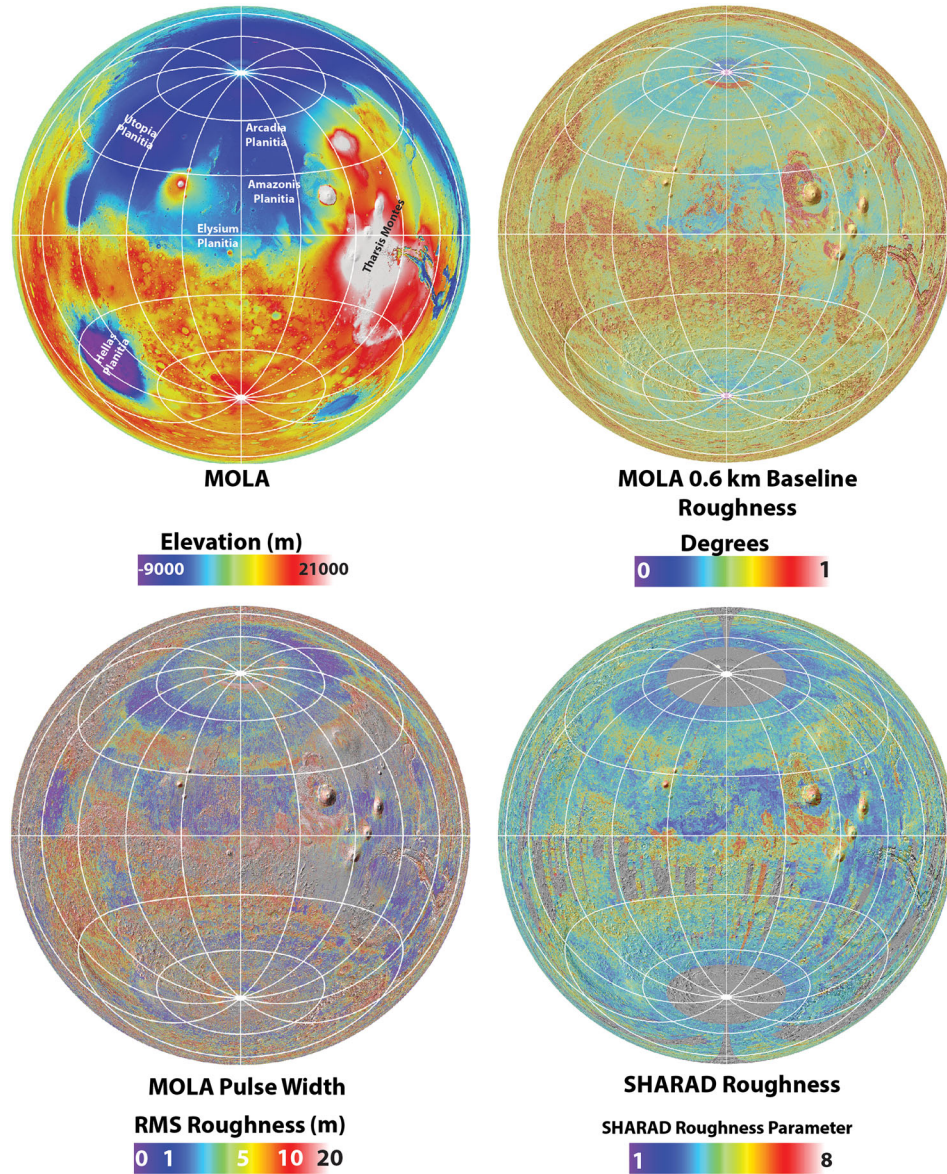


Figure 5. Maps of MOLA topography and roughness determined from 600 m MOLA baselines [Kreslavsky and Head, 2000], MOLA pulse width [Neumann *et al.*, 2003], and SHARAD data (this work). These measures of roughness are relevant to horizontal scales of order 100–1000 m for the MOLA point-to-point baseline measure, 1 m for MOLA pulse width, and 10–100 m for SHARAD ζ .

[28] If no other factors were important, the deviations from the mean of the roughness-corrected distribution would be due solely to changes in the surface Fresnel normal reflectivity ρ . As expected, the standard deviation of peak brightness declines after normalization to about 4.1 dB. The residual variability implies that the most reflective areas have ρ values a factor of 4–6 times greater than the mean reflectivity over the study region and that the least reflective areas have ρ values as low as 10% of this mean. The upper bound seems unreasonable for the difference between the reflectivity of a mixed rock and dust surface ($\rho = 0.10$ – 0.15) and bare rock ($\rho \sim 0.25$). We propose that the anomalously high values in this distribution are related to the role of coherent scattering, which can roughly double the peak-echo power [Campbell and Shepard, 2003]. This suggests that absolute estimation of the Fresnel reflectivity, based

on inference of the near-nadir scattering regime, is challenging [Grima *et al.*, 2012]. The lowest values of peak-echo reflectivity probably arise from two mechanisms. Where the local slope of the surface is on the order of a few degrees over scales comparable to the SHARAD footprint (a few hundred meters), the specular echo may be shifted out of the Doppler-resolved cells around the nadir point. This will tend to increase the roughness parameter and reduce the peak-echo power. The second mechanism is a relatively low near-surface density, at least over the top several meters, which reduces the Fresnel normal reflectivity of a target region.

[29] The SHARAD roughness parameter complements the MOLA 600 m baseline data, the shortest baseline of MOLA-derived roughness [Kreslavsky and Head, 2000, 2002]. The two datasets reveal broadly similar global distributions of roughness correlated with distinct geologic features and

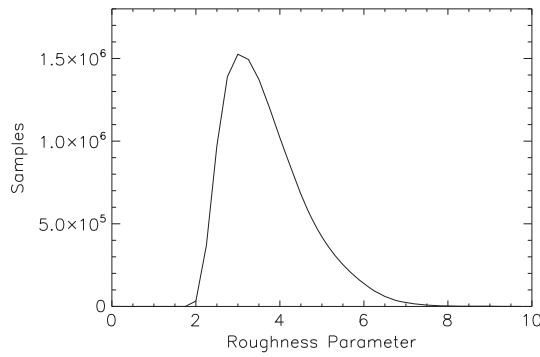


Figure 6. Histogram of SHARAD roughness parameter ζ over the region (70°S – 70°N , 0° – 360°E). Orbit tracks 2000–25999 used for compilation of these data, omitting any tracks collected in the rolled configuration.

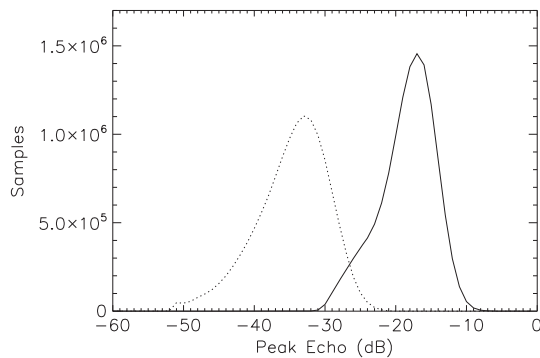


Figure 7. Histograms of uncompensated (dashed curve) and roughness-compensated (solid line) SHARAD peak-echo values, in dB, over the region (70°S – 70°N , 0° – 360°E). Note that roughness compensation reduces the overall spread in the echoes, leaving a distribution modulated primarily by the surface Fresnel reflectivity and/or coherent echoes from very smooth parts of the surface.

units (Figure 5). For example, the young volcanic plains of Elysium and Amazonis Planitiae are relatively smooth, whereas the Tharsis volcanoes are distinctly rougher. There are, however, profound differences associated with the two parameters being sensitive to roughness scales at least an order of magnitude apart: 10 m to 100 m for SHARAD ζ versus 100 s m to ~ 1000 m for the shortest MOLA baseline [Campbell *et al.*, 2003]. As a consequence, features of high topographic relief like the global dichotomy boundary and ancient basin ejecta are more prominent in the MOLA roughness data, while the SHARAD roughness parameter emphasizes more subtle texture related to geologic deposition and erosion mechanisms. Aeolian erosion features are particularly pronounced. For example, a patch of terrain in Arcadia Planitia with much greater roughness enhancement in the SHARAD map relative to the MOLA 600 m data is shown in Figure 8. Images from HiRISE show dense patterns of aeolian erosion within a friable deposit at the few-meter vertical scale, to which even the shortest MOLA baseline values are relatively insensitive. This comparison highlights how the two approaches to characterizing roughness offer alternative information for geologic studies, especially at the regional and local scales.

4.2. Latitude-Dependent Mantle

[30] *Mustard et al.* [2001] used Mars Orbiter Camera (MOC) images to identify a widespread mantling deposit poleward of 30° latitude in both hemispheres of Mars. Morphologic studies indicated that this unit was smooth at high latitudes and became increasingly dissected towards the equator, interpreted to result from loss of a significant volatile component. Studies of MOLA roughness statistics demonstrated the latitudinal dependence of the mantling deposits, which smooth the background terrain over hundreds of meters and larger horizontal scales [Kreslavsky and Head, 2000, 2002]. The combination of these datasets provided the basis of the hypothesis that the deposits represent the remnants of hemispherical ice sheets accumulated during a recent “ice age” initiated by periods of high obliquity [Head *et al.*, 2003].

[31] The SHARAD data provide additional weight to the ice-age hypothesis. To explore the latitudinal influence on roughness, we concentrated on the Arabia-Noachis Terrae hemisphere of Mars (0° to 40°E longitude). This region is optimal because it has SHARAD coverage in both hemispheres and does not contain any large-scale geologic features with specific roughness properties, such as the Medusae Fossae formation (see next section) or major volcanic, tectonic or impact landforms. Latitudinal averaging of the roughness parameter across this longitude band shows broad agreement with the MOLA roughness data (interquartile width of the frequency distribution of the differential slope at the 0.6 km baseline) (Figure 9). This correspondence further supports the occurrence of smoothing at latitudes poleward of $\sim 40^{\circ}$ that has been attributed to the presence of an ice-rich mantling unit [Kreslavsky and Head, 2000, 2002]. The smoothing is more pronounced in the northern hemisphere, which may reflect the ability of the mantling process to more readily mute features in the boreal plains with inherently lower roughness than those in the southern highlands.

[32] Two peaks of high roughness values are centered in the midlatitudes of each hemisphere (Figure 9). The northern peak is centered just south of Deuteronilus Mensae—the most topographically dramatic region of the dichotomy boundary. The lack of correlation of the northern peak with Deuteronilus Mensae itself and the occurrence of a second peak not associated with a distinct geologic unit in the southern hemisphere (Figure 9) suggests that these peaks are also climate related. The peaks broadly correlate with the MOC image survey of dissected mantle compiled by *Mustard et al.* [2001], potentially demonstrating that SHARAD is sensitive to the diagnostic texture of such terrain. Increasing the midlatitude coverage of the SHARAD dataset in the southern hemisphere will be important in assessing whether the trends observed are global in nature and to making further comparisons with the MOLA-derived roughness parameters pertaining to the mantling deposits.

4.3. The Medusae Fossae Formation

[33] The Medusae Fossae Formation (MFF) comprises a series of deposits along the highland boundary with Elysium and Amazonis Planitiae (Figure 10a). These deposits typically form elongate mesas or ridges, with ubiquitous aeolian features that suggest substantial erosion of an originally more extensive unit [Scott and Tanaka, 1986; Greeley and Guest, 1987]. The

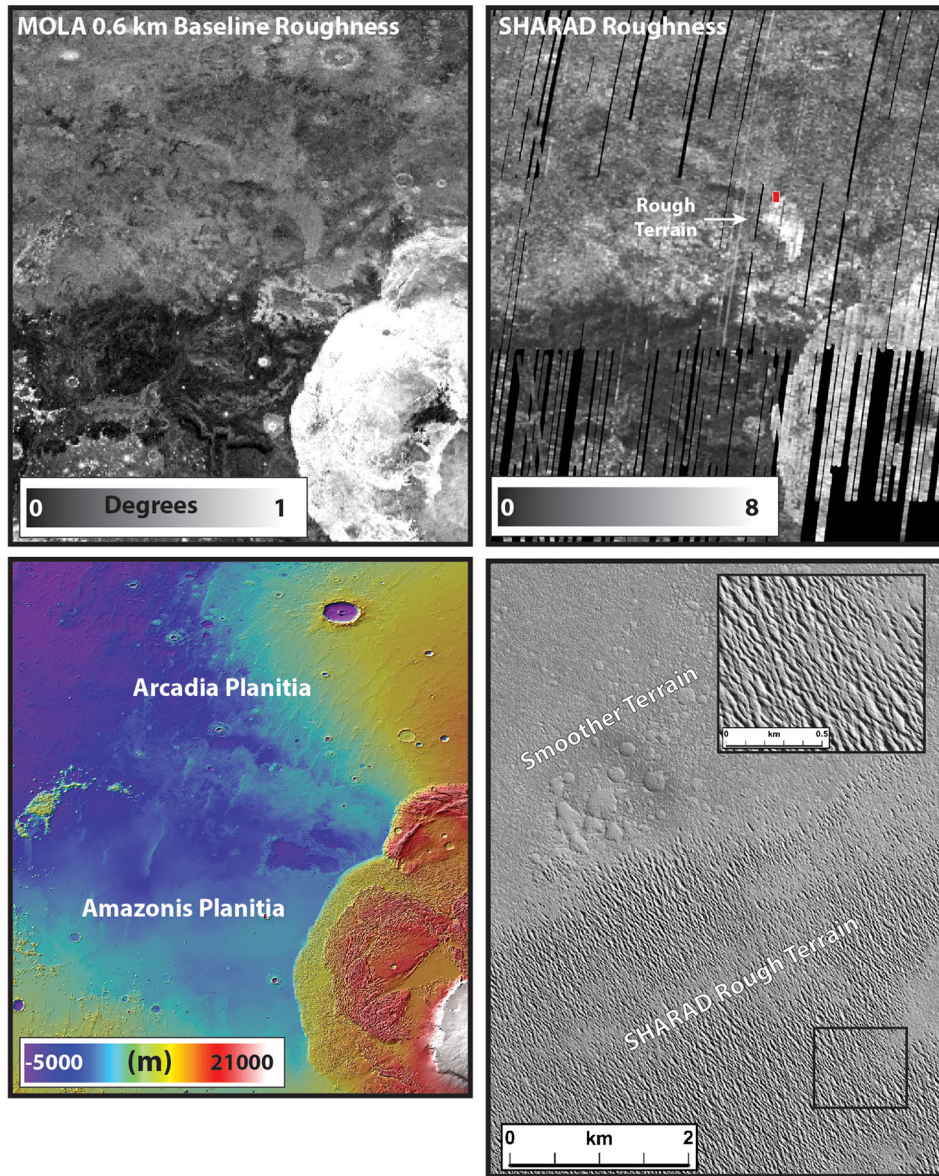


Figure 8. Comparison of MOLA 600 m roughness statistics and SHARAD roughness parameter for the region northwest of Olympus Mons, illustrated by the MOLA color shaded-relief image at lower left. Note the small patch of rough terrain labeled in the SHARAD image; this region has much less contrast with the plains in the 600 m baseline data. Red box shows location of the HiRISE image at lower right. The sounder measurements are detecting roughness at the few-meter to tens of meter scales associated with aeolian landforms such as those in the HiRISE image at lower right (PSP_006562_2235_RED).

formation mechanism of the MFF remains uncertain, but the favored scenario is a fine-grained, airfall deposit generated by volcanic activity in conjunction with groundwater [e.g., Bradley *et al.*, 2002]. Outlying deposits similar to the larger sections of the MFF are noted in the southern highlands, consistent with either a greater original extent or aeolian transport of material eroded from an initial deposit to the north [Harrison *et al.*, 2010]. The age of the overall formation had been assigned to the Amazonian period based on crater statistics [Scott and Tanaka, 1982], but recent work suggests that the deposits are significantly older (Hesperian period), and at least some current parts were formed by erosion, transport, and reworking of the initial material [Kerber and Head, 2010; Zimbelman and Scheidt, 2012].

[34] The MFF lies within a region of Mars termed Stealth for its very low radar backscatter in Earth-based images at 3.5 cm wavelength [Muhleman *et al.*, 1991]. This low return is attributed to fine-grained mantling due to wind transport of material eroded from the MFF deposits [Edgett *et al.*, 1997]. Supporting the notion of a friable, easily wind-eroded unit, radar sounding reveals that MFF materials have a real dielectric constant of 2.9 ± 0.4 , similar to that of the uppermost lunar regolith [Watters *et al.*, 2007; Carter *et al.*, 2009]. Microwave loss tangents are also low, estimated at 0.002 to 0.006 from MARSIS data [Watters *et al.*, 2007]. The broader Stealth region, characterized by low backscatter at much shorter wavelengths, is not evident in either SHARAD roughness or peak-echo maps

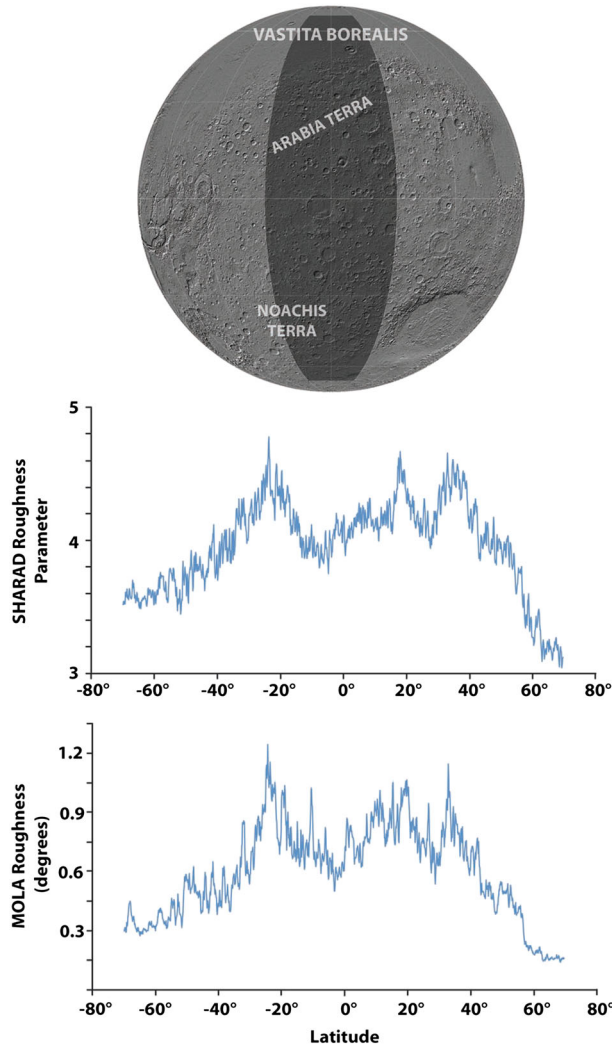


Figure 9. Latitude dependence of SHARAD and MOLA-derived roughness across the Arabia Terra and Noachis Terra regions of Mars (70°S–70°N, 0°–40°E). Top: MOLA hillshade data highlighting the region over which the roughness data were averaged. Middle: Plot of SHARAD roughness parameter averaged for each degree of latitude. Bottom: Plot of average MOLA roughness data (interquartile width of the frequency distribution of the differential slope at the 0.6 km baseline, see Kreslavsky and Head, 2000, 2002), spatially filtered to match the SHARAD footprint coverage. Note the generally good agreement between the two plots.

(Figure 10), consistent with a deposit that is too thin to obscure relief on the scale of a few meters.

[35] SHARAD data (Figure 10b) show that mesa- and ridge-like MFF features have moderate to high surface roughness, consistent with visible images showing abundant wind-carved yardangs and grooves [e.g., Harrison *et al.*, 2010]. Peak-echo strength for any given site, as expected, declines with increasing roughness. There is substantial variability, however, in both roughness and peak-echo behavior among the major MFF deposits. For example, the outer margins of the Eumenides Dorsum and Amazonis Mensa deposits are much rougher than their interior areas. Perhaps the most striking case is Gordii Dorsum. Northwest of the mapped division between the upper

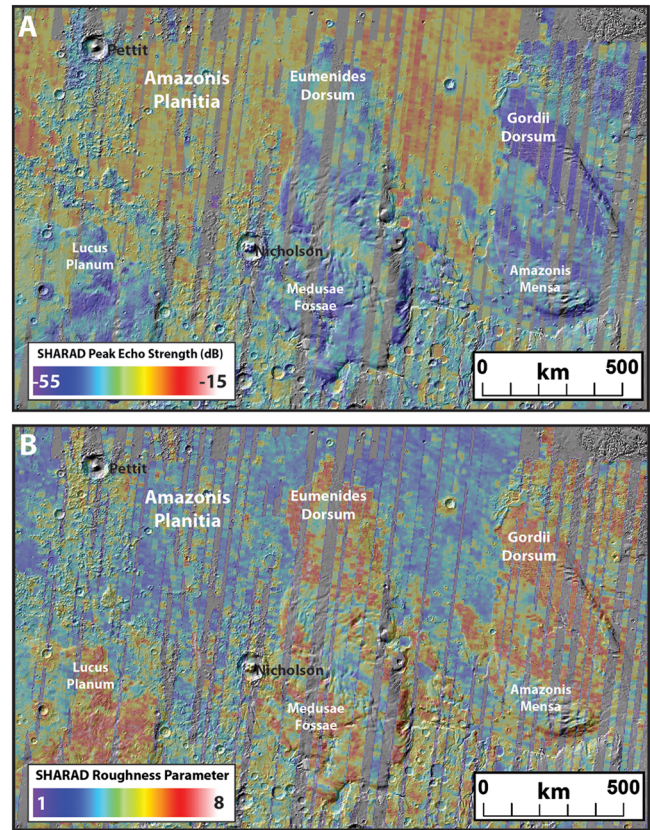


Figure 10. (a) Image of SHARAD peak-echo strength, as color overlay on MOLA hillshade, of the eastern Medusae Fossae Formation (MFF) (10°S–15°N, 182°–220°E), in logarithmic (dB) scale. (b) SHARAD roughness parameter for the study region, as color overlay on MOLA hillshade. Note the generally high roughness of all large MFF deposits (Gordii Dorsum, Amazonis Mensa, Eumenides Dorsum, and Lucus Planum).

and middle units of the MFF (“Amu” and “Amm” units of Scott and Tanaka [1986]), the peak echo drops more dramatically with roughness than in other instances of MFF terrain. Figure 11 shows a SHARAD track that crosses Gordii Dorsum and Amazonis Mensa, illustrating the very weak echo power from the former deposit. MRO CTX images near the SHARAD ground track (Figure 12) show the significant difference in wind-eroded morphology between the two units. The surface of Gordii Dorsum is dissected on horizontal and vertical scales of order 100 m, in contrast to much smaller (10 m scale) vertical relief in Amazonis Mensa. The highly eroded surface is a major reason for the lower SHARAD echo power over Gordii Dorsum, but this drop exceeds that noted for other rough parts of the equatorial region.

[36] We quantify this difference by examining deviations from the average dependence of SHARAD peak echo on the roughness parameter, ς (Figure 13). The regional-average curve in this figure shows the expected decline in peak backscatter power with increasing roughness (equation (6)). This plot also highlights the dominant role of roughness changes, which account for >20 dB of variation in the peak-echo strength, relative to the maximum 3–6 dB range of brightness induced by the expected span of surface Fresnel reflectivity.

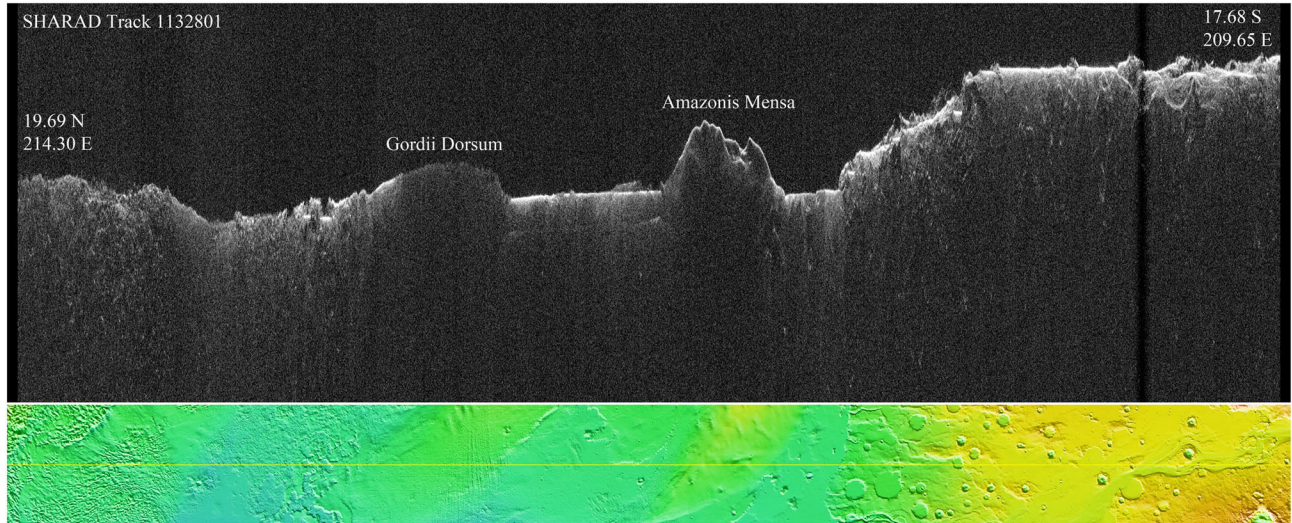


Figure 11. SHARAD track 1132801 (upper panel), with ground-track trace shown as yellow line on MOLA color shaded-relief image (lower panel). Radargram vertical extent is $55.95\ \mu\text{s}$ (about 8.4 km in free space). Note the very low echo power from the surface of the Gordii Dorsum part of the Medusae Fossae Formation, relative to that from Amazonis Mensa.

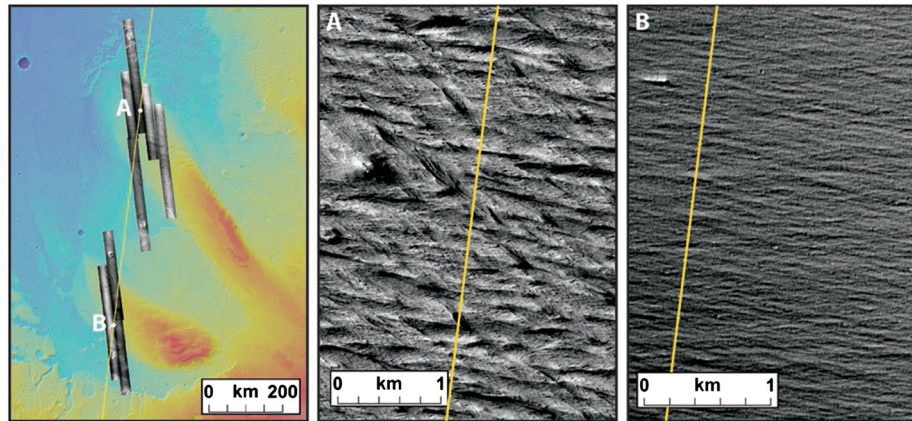


Figure 12. CTX images of Gordii Dorsum (center panel) and Amazonis Mensa (right panel) regions of the Medusae Fossae Formation, near the ground trace of SHARAD track 1132801 (left panel, showing CTX coverage and locations of images A and B).

Values from the Eumenides region of the MFF fall very close to the regional trend, while the peak echo for the northwestern part of the Gordii Dorsum deposit is at least 6 dB (a factor of 4) lower than the average for similar ζ values. As noted above, both surface slopes and bulk reflectivity (density) changes can lead to reduced peak-echo power.

[37] We examined local slope effects by comparing Gordii Dorsum surface echoes between the standard 11 s synthetic aperture and a 33 s integration time. The larger aperture integrates echoes from a broader range of surface scattering angles, but we find that returns from Gordii Dorsum show no evidence for strong specular echoes from tilted features. While the deeply incised surface must have some effect on the peak returns, it appears that surface reflectivity also plays a role. If we take the typical relationship of real dielectric constant to density, d , as 1.96^d [Carrier *et al.*, 1991], then the change in Fresnel normal reflectivity requires a maximum factor-of-two offset between the average regional surface density

(e.g., $2.5\ \text{g/cm}^3$) and that of Gordii Dorsum (e.g., $1.2\ \text{g/cm}^3$). The depth to which this low-density behavior persists is not well constrained but is at least several meters. As a comparison, Watters *et al.* [2007] estimated a bulk density of $1.4\text{--}1.8\ \text{g/cm}^3$ integrated over the full thickness of parts of the MFF. Examples of low-peak SHARAD echoes also occur for mound-like deposits in the floors of some highland craters. Figure 14 shows a SHARAD track that crosses a 43 km-diameter crater centered at 5.13°S , 221.06°E , which has an interior mound of wind-eroded material (Figure 15). Other craters with such interior deposits exhibit the same behavior, suggesting a low near-surface density consistent with possible emplacement as reworked debris eroded from other parts of the Medusae Fossae Formation.

4.4. Pavonis Mons Fan Deposits

[38] The large volcanoes of the Tharsis rise have fan-shaped deposits or aprons of material extending from the slope break

near the base of each edifice. These deposits are preferentially located on the northwest sides of Pavonis, Ascræus, and Arsia Montes. The surface morphology within the fans ranges from “smooth” to “knobby” to “ridged” facies [Scott *et al.*, 1998]. Based on the similarity of the arcuate ridges to terrestrial post-glacial features like drop moraines and on the apparent superposition of smooth-facies units on the knobby terrain, some authors suggest that the fan-shaped deposits reflect the remnant deposits of episodic glacial activity during periods

of high obliquity and that perhaps some of the smooth-facies units retain an ice core beneath an insulating lag [Head and Marchant, 2003; Shean *et al.*, 2005].

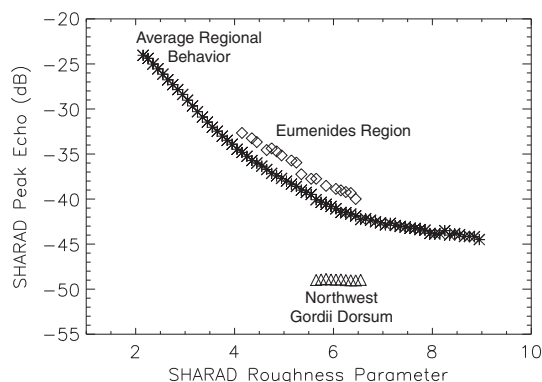


Figure 13. SHARAD peak-echo strength versus roughness parameter for Elysium Planitia and nearby highlands (asterisks) [9.7°S–16.9°N, 181.3–218.8°E]. This average curve shows the expected decline in peak backscatter power as the surface roughness increases. Also plotted are data for the Eumenides region [7.6°N–10.5°N, 198.2–202.6°E] (diamonds) and northwest Gordii Dorsum (triangles) [6.1°N–8.2°N, 211.3–213.2°E].

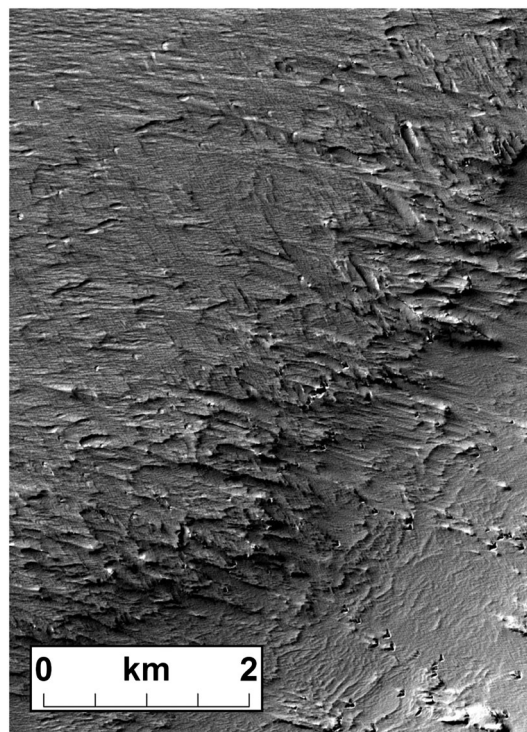


Figure 15. MRO Context Camera (CTX) image of mound-like deposit in the floor of the 43 km-diameter crater highlighted in Figure 14.

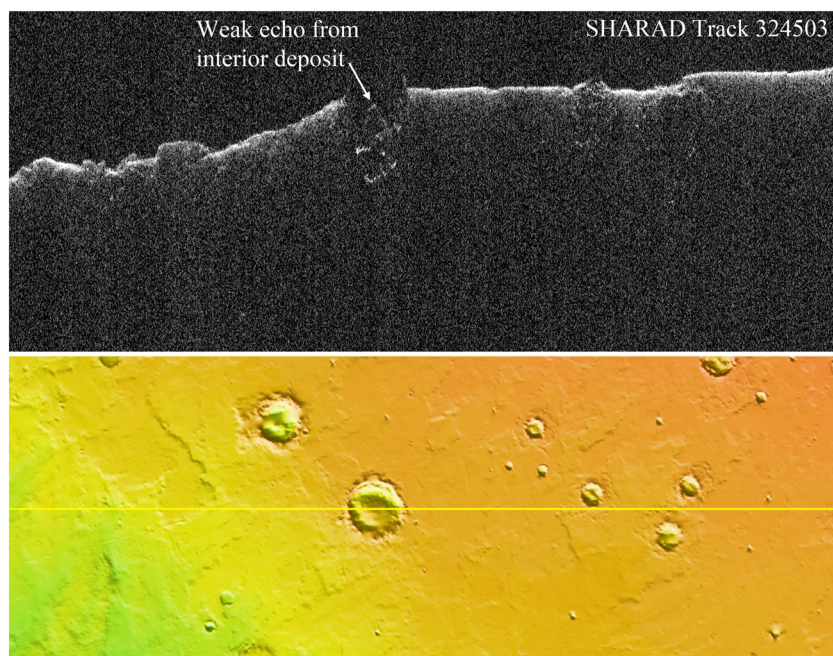


Figure 14. Portion of SHARAD track 324503 (upper panel), crossing a 43 km-diameter crater centered at 5.13°S, 221.06°E. Image width is 562 km; radargram vertical extent is 37.5 μ s (about 5.63 km in free space). Lower panel shows the orbit ground track trace as a yellow line on a MOLA color shaded-relief image. Note the very low SHARAD echo power from the mound-like deposit in the crater floor.

[39] SHARAD data show that the Arsia Mons fan deposit and flow fields are rough, at the few-meter to decameter scale, over a large region north and northwest of the volcano (Figure 16). There is also a distinct wedge-shaped smooth region on the east flank of Arsia Mons, and the summit caldera region is quite flat (low roughness, high peak echo). The Ascraeus Mons northern flank is much rougher relative to the southern flank in SHARAD results, where the MOLA 600 m data [Kreslavsky and Head, 2000] show a more homogeneous signature. Caution must be used in inferring density variations from the peak-echo data for the volcanoes because the flank slopes can be large enough to cause a significant reduction in reflected signal. We focus here on analysis of SHARAD data for Pavonis Mons and in particular the smoothest regions near the northern margin of the volcano.

[40] The Pavonis Mons smooth facies “embay and partially bury” [Scott *et al.*, 1998] the knobby and ridged facies. Shean *et al.* [2005] estimate thicknesses from MOLA data of up to 500–600 m for some lobes of the Pavonis smooth material, and suggest that the separate units were once part of a contiguous, larger deposit. Numerous SHARAD observations were targeted to study this unit, based on the finding that some smaller lobate debris aprons with surface structures associated with glacial flow appear to have low microwave loss consistent with residual interior ice [Plaut *et al.*, 2009; Holt *et al.*, 2008]. Some of these sounding observations were made in the MRO rolled configuration to improve signal-to-noise performance by up to 6 dB over the nadir-oriented mode.

[41] No SHARAD observations to date show a basal interface or internal layering for the Pavonis Mons “smooth facies” region (Figure 17). Likewise, the few MARSIS tracks that pass directly over the thickest part of the fan do not show subsurface reflecting horizons. We suggest two possible scenarios to explain this significant difference from mantling materials like the MFF [Carter *et al.*, 2009] and the radar-transparent lobate debris aprons [Holt *et al.*, 2008]. First, the smooth facies may be a relatively thin veneer (less than perhaps 50 m) capping the knobby facies as it increases in elevation toward the volcano flank. Evidence for this comes from HiRISE images of small cones or domes being exhumed from even the apparently thickest (highest elevation) parts of the smooth facies (Figure 18). Such a thin deposit implies minimal current ice content for the smooth facies, perhaps even the complete sublimation of volatiles from the final glacial remnant.

[42] The second scenario is that the smooth facies are hundreds of meters thick at their maximum, per Shean *et al.* [2005], but that they are formed of essentially homogeneous, poorly consolidated material. The lack of a distinct reflecting interface at the base of the unit might be due to the similar density properties of the knobby facies beneath, in contrast to the strong dielectric contrast between the MFF materials and the underlying lava plains [Watters *et al.*, 2007; Carter *et al.*, 2009]. The rugged structure of the knobby facies at several-meter and larger scales (Figure 17) would further reduce the reflection from such an interface. In this scenario, the lack of internal layering suggests that no discrete ice core exists within the uppermost unit of the Pavonis Mons fan-shaped deposit. The overall volume of fine material required to account for a thick smooth facies argues against its origin as a sublimation remnant of the final glacial period and may be more consistent with a

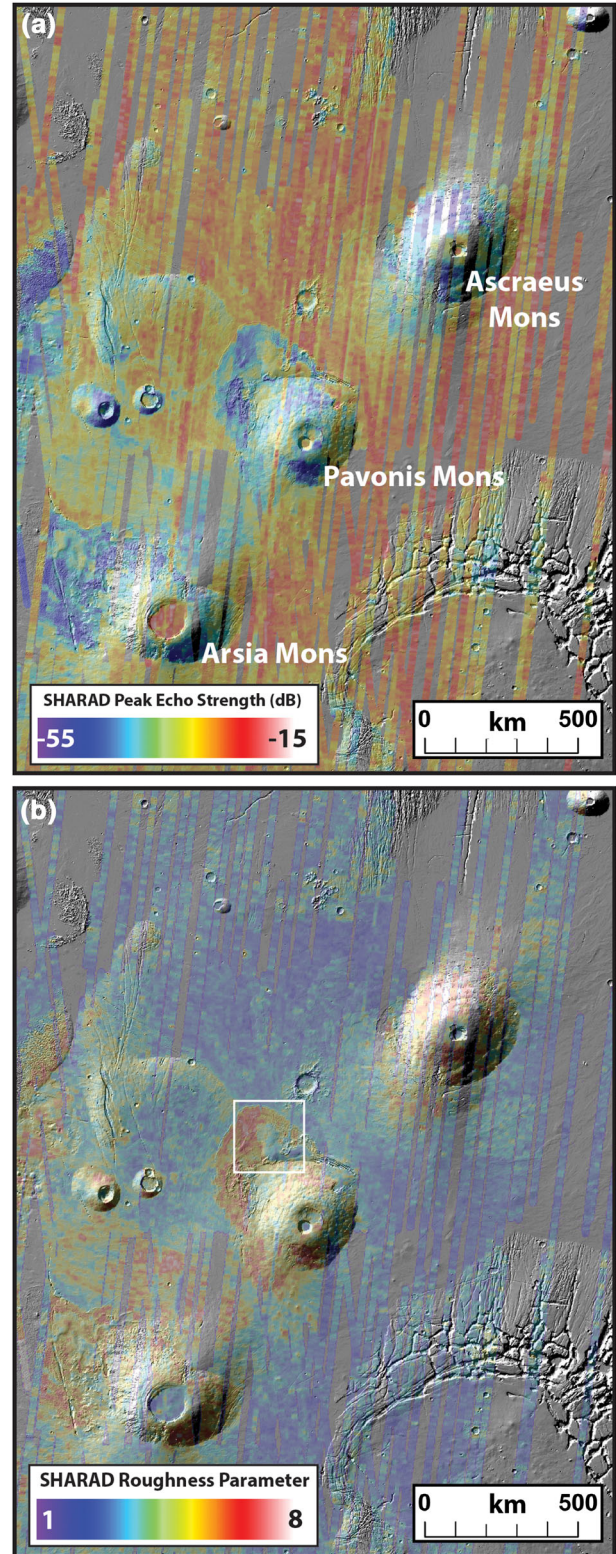


Figure 16. (a) Image of SHARAD peak-echo strength, as color overlay on MOLA hillshade, of Tharsis Montes region (18.0°S–25.0°N, 230°–265°E), in logarithmic (dB) scale. (b) SHARAD roughness parameter for the study region, as color overlay on MOLA hillshade. White box shows approximate location of study area in Figure 17.

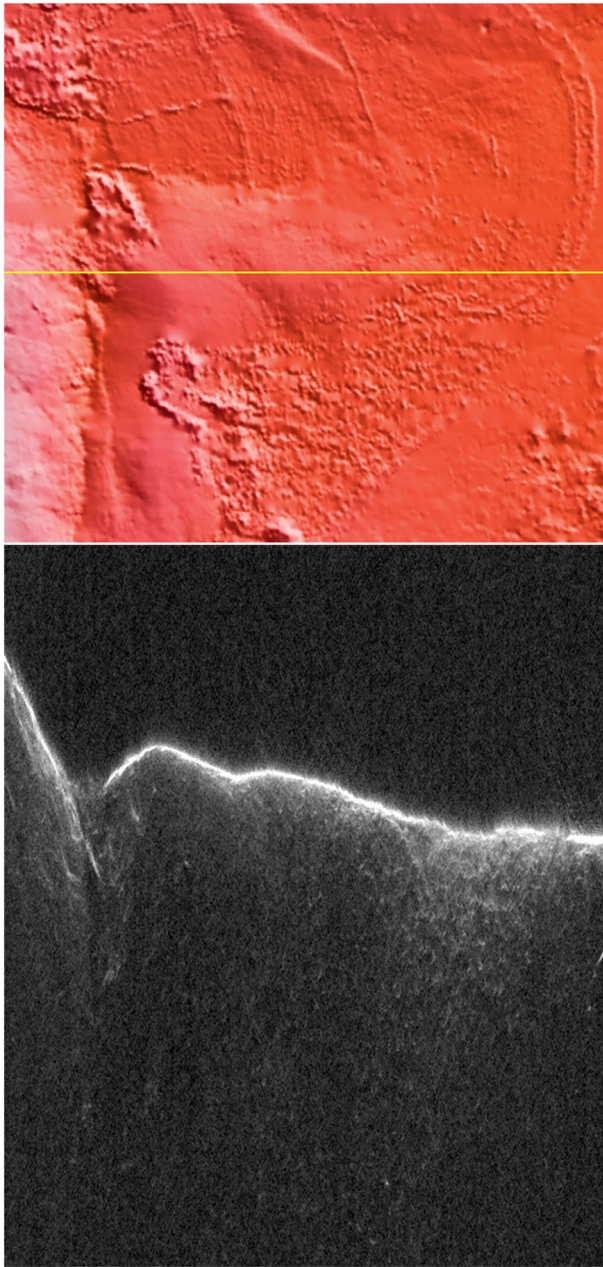


Figure 17. SHARAD radargram (bottom) and MOLA color shaded-relief image (top) for portion of Track 1962801. Sounder track is shown as yellow line across MOLA topography image. Image width is about 230 km. MRO was rolled about 25° for this observation, so the signal-to-noise ratio is as high as possible for the sounder. Radargram vertical extent is $45\mu\text{s}$ (about 6.8 km in free space). Note the strong off-nadir signals (below the surface return) from the knobby facies at right of the sounder track.

separate formation mechanism such as interaction between magma and ground ice.

5. Summary and Implications for Future Work

[43] The SHARAD-derived roughness values complement those obtained from MOLA pulse-width measurements and along-track MOLA profile analysis. The characterization of

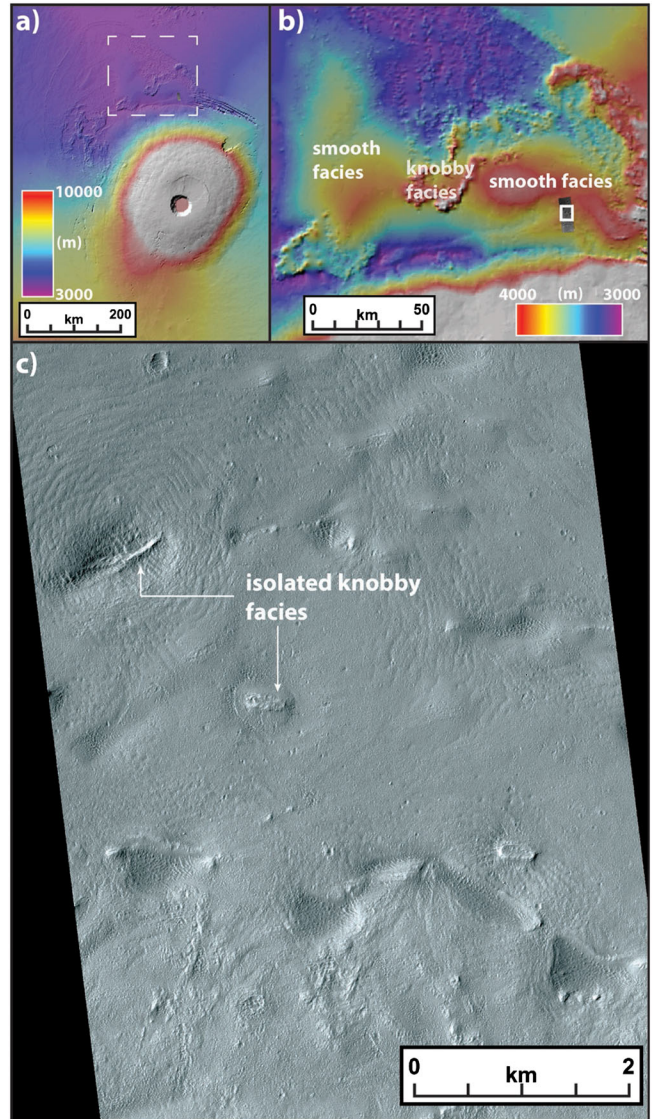


Figure 18. (a) MOLA color topography image of Pavonis Mons and northwestern fan-shaped deposits. (b) Detail of MOLA topography (outline in Figure 18a) near the northern volcano flank. Inset box shows location of HiRISE image. (c) HiRISE image (portion of ESP_018995_1845) showing isolated knobs and ridges exhumed by erosion of the smooth-facies material near the highest elevations on the lobate apron.

surface-roughness properties can be extended through comparison of these few-meter-scale to kilometer-scale parameters with the decimeter-scale roughness and shallow subsurface penetration capability of Earth-based 12.6 cm radar data [Harmon *et al.*, 1999, 2012]. Further analysis of SHARAD roughness and peak-echo data may identify additional areas mantled by low-density deposits, as illustrated by our Gordii Dorsum and infilled-crater examples. Studies of the distribution of roughness over the Tharsis Montes and other lobate aprons provide context for the interpretation of sounding data and constraints on the presence of remnant ice. On the global scale, the SHARAD roughness maps provide new insights on the distribution and nature of possibly volatile-rich mantling material.

[44] Of particular future interest is the possibility for using SHARAD-derived roughness maps of the northern plains to locate areas with strongly contrasting, but shallow, dielectric interfaces. A preliminary study offered hints of reflections in the SHARAD data [Putzig *et al.*, 2009], but these returns occur at delay times that coincide with the strong sidelobe pattern of the sounder echoes. It is possible that the presence of shallow interfaces within this delay region can be identified by anomalous enhancements of the roughness parameter. The key aspect is to have a measure of the surface roughness from other datasets, such as High Resolution Stereo Camera (HRSC)-derived digital elevation models against which to compare the SHARAD roughness map. This type of integrative study, and the extension of the SHARAD roughness technique to the polar layered deposits, offers a new window on surface and near-surface properties across Mars.

[45] **Acknowledgments.** The authors thank two anonymous reviewers for their constructive comments. Funding for this work was provided in part by the NASA Mars Reconnaissance Orbiter project. The Shallow Radar (SHARAD) was provided by the Italian Space Agency, and its operations are led by the Department of Information Engineering, Electronics, and Telecommunications, University of Rome “La Sapienza.”

References

- Barrick, D. E., and W. H. Peake (1967), Scattering from surfaces with different roughness scales: Analysis and interpretation, Ohio State University Electroscience Laboratory Report 1388-26.
- Bradley, B. A., S. E. H. Sakimoto, H. Frey, and J. R. Zimbelman (2002), Medusae Fossae Formation: New perspectives from Mars Global Surveyor, *J. Geophys. Res.*, **107**, doi:10.1029/2001JE001537.
- Campbell, B. A., L. M. Carter, R. J. Phillips, J. Plaut, N. Putzig, A. Safaeinili, R. Seu, D. Biccari, A. Egan, and R. Orosei (2008), SHARAD radar sounding of the Vastitas Borealis formation in Amazonis Planitia, *J. Geophys. Res.*, **113**, E12010, doi:10.1029/2008JE003177.
- Campbell, B. A., L. M. Carter, N. E. Putzig, and R. J. Phillips (2011), Autofocus correction of phase distortion effects on SHARAD echoes, *IEEE Geosci. Remote Sens. Lett.*, **PP(99)**, 939–942, doi:10.1109/LGRS/2011.2143692.
- Campbell, B. A., R. R. Ghent, and M. K. Shepard (2003), Limits on inference of Mars small-scale roughness from MOLA data, *Geophys. Res. Lett.*, **30**(3), 1115, doi:10.1029/2002GL016550.
- Campbell, B. A., and N. E. Putzig (2011), Surface roughness maps of Mars based on SHARAD echoes, *Lun. Plan. Sci. Conf.* 42, abs. 1489.
- Campbell, B. A., and M. K. Shepard (2003), Coherent and incoherent components in near-nadir radar scattering: Applications to Mars radar sounding, *J. Geophys. Res.*, **108**(E12), 5132, doi:10.1029/2003JE002164.
- Carrier, W. D., G. R. Olhoeft, and W. Mendell (1991), Physical properties of the lunar surface, in *Lunar Sourcebook*, 756 pp., Cambridge Univ. Press, New York.
- Carter, L. M., et al. (2009), Shallow Radar (SHARAD) sounding observations of the Medusae Fossae Formation, Mars, *Icarus*, **199**, 295–302.
- Croci, R., R. Seu, E. Flamini, and E. Russon (2011), The SHARAD (SHARAD) onboard the NASA MRO mission, *Proc. IEEE*, **99**, 794–807, doi:10.1109/JPROC.2010.2104130.
- Cumming, I. G., and F. H. Wong (2005), Digital Processing of Synthetic Aperture Radar Data, 625 pp, Artech House, Boston, MA.
- Edgett, K. S., B. J. Butler, J. R. Zimbelman, and V. E. Hamilton (1997), Geologic context of the Mars radar “Stealth” region in southwestern Tharsis, *J. Geophys. Res.*, **102**, 21,545–21,567.
- Ford, P. G., and G. H. Pettengill (1992), Venus topography and kilometer-scale slopes, *J. Geophys. Res.*, **97**, 13,102–13,114.
- Greeley, R., and J. E. Guest (1987), Geologic map of the eastern equatorial region of Mars, USGS I-1802-B.
- Grima, C., W. Kofman, A. Hérique, R. Orosei, and R. Seu (2012), Quantitative analysis of Mars surface radar reflectivity at 20 MHz, *Icarus*, **220**, 84–99, doi:10.1016/j.icarus.2012.04.017.
- Hagfors, T. (1964), Backscattering from an undulating surface with applications to radar returns from the Moon, *J. Geophys. Res.*, **69**, 3779–3784.
- Harmon, J. K., R. E. Arvidson, E. A. Guinness, B. A. Campbell, and M. A. Slade (1999), Mars mapping with delay-Doppler radar, *J. Geophys. Res.*, **104**, 14,065–14,090.
- Harmon, J. K., M. C. Nolan, D. I. Husmann, and B. A. Campbell (2012), Arecibo radar imagery of Mars: The major volcanic provinces, *Icarus*, **220**, 990–1030, doi:10.1016/j.icarus.2012.06.030.
- Harrison, S. K., M. R. Balme, A. Hagermann, J. B. Murray, and J.-P. Muller (2010), Mapping Medusae Fossae Formation materials in the southern highlands of Mars, *Icarus*, **209**, 405–415, doi:10.1016/j.icarus.2010.04.016.
- Head, J. W., and D. R. Marchant (2003), Cold-based mountain glaciers on Mars: Western Arsia Mons, *Geology*, **31**, 641–644.
- Head, J. W., J. F. Mustard, M. A. Kreslavsky, R. E. Milliken, and D. R. Marchant (2003), Recent ice ages on Mars, *Nature*, **426**, 797–802.
- Holt, J. W., et al. (2008), Radar sounding evidence for buried glaciers in the southern mid-latitudes of Mars, *Science*, **322**, 1235–1238, doi:10.1126/science.1164246.
- Kerber, L., and J. W. Head (2010), The age of the Medusae Fossae Formation: Evidence of Hesperian emplacement from crater morphology, stratigraphy, and ancient lava contacts, *Icarus*, **206**, 669–684, doi:10.1016/j.icarus.2009.10.001.
- Kreslavsky, M. A., and J. W. Head (2000), Kilometer-scale roughness of Mars: Results from MOLA data analysis, *J. Geophys. Res.*, **105**, 26,695–26,711.
- Kreslavsky, M. A., and J. W. Head (2002), Mars: Nature and evolution of young latitude-dependent water-ice-rich mantle, *Geophys. Res. Lett.*, **29**, doi:10.1029/2002GL015392.
- Mouginot, J., W. Kofman, A. Safaeinili, C. Grima, A. Hérique, and J. J. Plaut (2009), MARSIS surface reflectivity of the south residual cap of Mars, *Icarus*, **201**, 454–459, doi:10.1016/j.icarus.2009.01.009.
- Muhleman, D. O., B. J. Butler, A. W. Grossman, and M. A. Slade (1991), Radar images of Mars, *Science*, **253**, 1508–1513.
- Mustard, J. F., C. D. Cooper, and M. K. Rifkin (2001), Evidence for recent climate change on Mars from the identification of youthful near-surface ground ice, *Nature*, **412**, 411–414.
- Neumann, G. A., J. B. Abshire, O. Aharonson, J. B. Garvin, X. Sun, and M. T. Zuber (2003), Mars Orbiter Laser Altimeter pulse width measurements and footprint-scale roughness, *Geophys. Res. Lett.*, **30**, 1561, doi:10.1029/2003GL017048.
- Plaut, J. J., A. Safaeinili, J. W. Holt, R. J. Phillips, J. W. Head, R. Seu, N. E. Putzig, and A. Frigeri (2009), Radar evidence for ice in lobate debris aprons in the mid-northern latitudes of Mars, *Geophys. Res. Lett.*, **36**, L2203, doi:10.1029/2008GL036379.
- Putzig, N. E., Phillips, R. J., Head, J. W., Mellon, M. T., Campbell, B. A., Egan, A. F., Plaut, J. J., Carter, L. M., and the SHARAD Team (2009), Do shallow radar soundings reveal possible near-surface layering throughout the northern lowlands of Mars?, *Lunar and Plan. Sci. Conf.* 40, abstract 2477.
- Safaeinili, A., W. Kofman, J. Mouginot, Y. Gim, A. Hérique, A. B. Ivanov, J. J. Plaut, and G. Picardi (2007), Estimation of the total electron content of the Martian ionosphere using radar sounder surface echoes, *Geophys. Res. Lett.*, **34**, L23204, doi:10.1029/2007GL032154.
- Scott, D. H., J. M. Dohm, and J. R. Zimbelman (1998), Geologic map of Pavonis Mons Volcano, Mars, USGS I-2561.
- Scott, D. H., and K. L. Tanaka (1982), Ignimbrites of Amazonis Planitia region of Mars, *J. Geophys. Res.*, **87**(B2), 1179–1190.
- Scott, D. H., and K. L. Tanaka (1986), Geologic map of the western equatorial region of Mars, USGS I-1802-A.
- Seu, R., et al. (2007), The SHARAD sounding radar on MRO, *J. Geophys. Res.*, doi:10.1029/2006JE002475.
- Shean, D. E., J. W. Head, and D. R. Marchant (2005), Origin and evolution of a cold-based tropical mountain glacier on Mars: The Pavonis Mons fan-shaped deposit, *J. Geophys. Res.*, **110**, E05001, doi:10.1029/2004JE002360.
- Shepard, M. K., R. A. Brackett, and R. E. Arvidson (1995), Self-affine (fractal) topography: Surface parameterization and radar scattering, *J. Geophys. Res.*, **100**, 11709–11718.
- Shepard, M. K., B. A. Campbell, M. Bulmer, T. Farr, L. R. Gaddis, and J. Plaut (2001), The roughness of natural terrain: A planetary and remote sensing perspective, *J. Geophys. Res.*, **106**, 32,777–32,795.
- Simpson, R. A., J. K. Harmon, S. H. Zisk, T. W. Thompson, and D. O. Muhleman (1992), Radar determination of Mars surface properties, in *Mars*, edited by H. Kieffer, B. Jakosky, C. Snyder, and M. Mathews, 1498 pp., Univ. of AZ Press, Tucson.
- Simpson, R. A., and G. L. Tyler (1982), Radar scattering laws for the lunar surface, *IEEE Trans. Antennas Propag.*, **AP-30**, 438–449.
- Tyler, G. L. (1979), Comparison of quasispecular radar scatter from the Moon with surface parameters obtained from images, *Icarus*, **27**, 29–45.
- Watters, T. R., et al. (2007), Radar sounding of the Medusae Fossae Formation Mars: Equatorial ice or dry, low-density deposits?, *Science*, **318**, 1125–1128.
- Zimbelman, J. R., and S. P. Scheidt (2012), Hesperian age for Western Medusae Fossae Formation, Mars, *Science*, **336**, 1683, doi:10.1126/science.1221094.